THE ASTRONOMICAL JOURNAL VOLUME 112, NUMBER 2 AUGUST 1996

ACCURATE SKY SUBTRACTION OF LONG-SLIT SPECTRA:[1] VELOCITY DISPERSIONS AT Σ_V=24.0 MAG/ARCSEC^2

KENNETH R. SEMBACH AND JOHN L. TONRY

Center for Space Research/Physics Department, M.I.T., Cambridge, Massachusetts 02139
Electronic mail: sembach@sundoggie.mit.edu, jt@antares.mit.edu

Received 1996 April 4; revised 1996 May 8

ABSTRACT

We describe an observing strategy for obtaining accurate sky subtraction when observing with a long-slit spectrograph. The technique is a chopping procedure in which the telescope is sequentially moved from object to sky on short time scales ($\approx$ 300 s), but instead of reading out the CCD detector with each exposure, we repeatedly clock the charge on the chip in the parallel direction in a manner that produces two complete exposures (one object+sky, one sky) on each CCD frame. The background subtraction proceeds naturally by differencing these two exposures. We show that this method provides superior results to more traditional sky-subtraction methods that rely on measuring the sky brightness at the ends of the slit. We find that we can reach a *V*-band surface brightness of $\approx$ 24 mag arcsec^{-2} in about 8 hours of observing time on the 2.4-meter Hiltner telescope at the Michigan–Dartmouth–MIT Observatory. We present some preliminary results obtained with this method for the stellar dynamics in the outer envelopes of three elliptical galaxies (M87, NGC 5846, and IC 1101). We use cross-correlation and Fourier quotient techniques to derive radial velocity and velocity dispersion profiles. We confirm that the velocity dispersion in the outer envelope of IC 1101 (the central galaxy in Abell 2029) rises with distance from the center of the galaxy, as noted by Dressler [APJ. 23, 659 (1979)].

1. INTRODUCTION

In this paper we describe a technique for doing accurate background subtraction for long-slit spectroscopy. To provide the best possible subtraction, it is necessary to measure the sky and object with the same detector pixels. This key point is often overlooked in long-slit studies, where necessity normally dictates that the sky information be taken from the ends of the slit. For extended objects that fill the slit, this is obviously a problem. However, it remains a problem for objects that do not fill the slit as well. There is usually some curvature in the projected image of the slit on the detector (introduced by the optics), and rectification of the slit image introduces errors in the background estimate measured from the slit ends. Furthermore, if the background and object are not measured with the same pixels, the flat fielding necessary in order to do accurate sky subtraction must be precise. These basic considerations are often the primary factors that dictate how faint an object can be to do quality long-slit spectroscopy in reasonable amounts of time.

2. THE OBSERVING STRATEGY

In the following discussion we assume that the observer is using a conventional CCD and that parallel charge transfer on the chip can be controlled through appropriate commands to the CCD electronics. A low-cost CCD system of this type has been described by Metzger *et al.* (1993). The observing strategy is a basic chopping procedure in which the spectrum of the astronomical object of interest and the sky background are measured with the same detector elements.

We begin by masking off two thirds of the CCD so that the inner third of the chip used for the observations is free of serious cosmetic blemishes and sees the full slit length required for the observations (Fig. 1a). This masking may be accomplished by either blocking the incoming light at the window of the CCD dewar or at the plane of the slit. We use a black, light resistant tape placed on the ends of the slit mechanism in combination with an adjustable slit decker to effectively darken the portion of the CCD that is not used for the science observations.

We then perform the following observing sequence. First, the galaxy is acquired and a suitable nearby star in the field of view is selected for guiding. The guider is enabled, CCD cleared, and a short ($\sim$ 300 s) spectrum of the galaxy taken (Fig. 1b). The shutter is closed, the guiding halted, and the charge on the CCD clocked in the parallel direction until the galaxy spectrum is under the mask furthest from the serial register of the chip. The telescope is offset to a predetermined "clear" sky position. For practical purposes, the sky offset is generally 10′– 20′ and is free of galaxies or stars bright enough to contaminate the slit. The shutter is opened and an exposure of equal duration to that obtained for the galaxy is taken of the sky (Fig. 1c). Next, the shutter is closed and the charge clocked in the parallel direction toward the serial register until the sky spectrum is under the second dark mask and the galaxy spectrum is placed in its original position (Fig. 1d). The guide star is re-acquired by the guider, which retains information about the previous location

[1]Based on observations conducted at the Michigan-Dartmouth-MIT Observatory.

 0004-6256/96/112(2)/797/9/$10.00

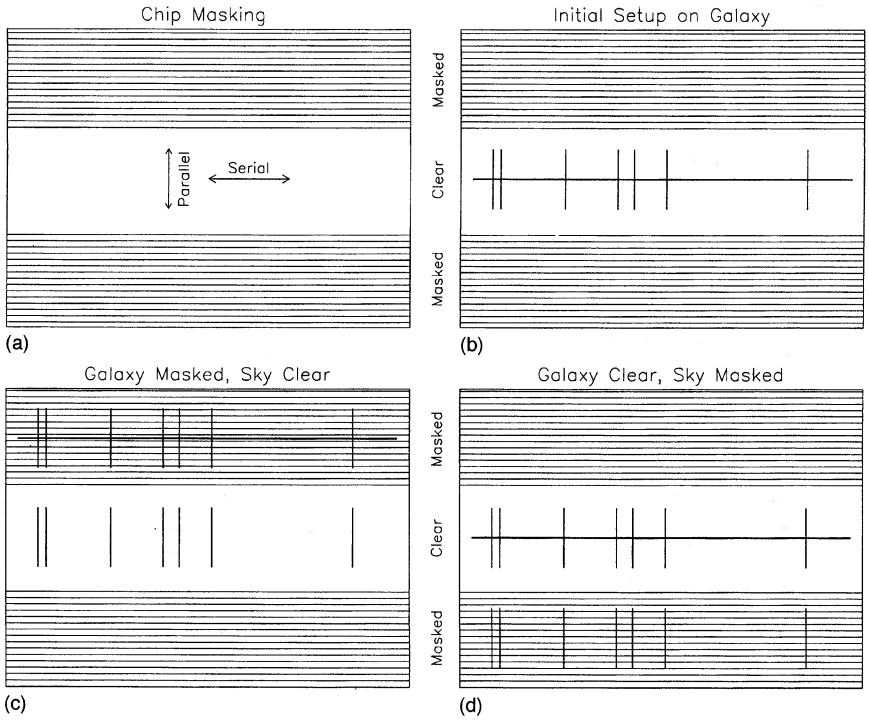

FIG. 1. A schematic of the observing strategy used in our observations. The upper left panel (a) shows the chip masking and clocking directions. The upper right panel (b) shows the placement of the galaxy spectrum on the chip after the first sub-exposure. The wavelength dispersion runs from left to right. The vertical lines represent night sky lines. The lower left panel (c) shows the spectra on the chip during the exposure of the clear sky field. The bottom right panel (d) shows the spectra on the chip after the galaxy has been recentered.

of the star, and the entire process is repeated as many times as desired before reading out the charge on the chip.

To perform this chopping sequence, it is necessary to shift the electric charge on the CCD between observations of the object and sky. For a CCD with good parallel charge transfer properties, this procedure is essentially noiseless. The usual read noise incurred in passing the charge through the serial register amplifier during readout cannot be avoided. However, by avoiding repeated readouts between each segment of the observation by charge shifting, we accumulate sufficient signal to be sky-noise, rather than read-noise, dominated at low surface brightnesses.

We normally spend 300 s per sub-exposure on both the object and sky and iterate five times before reading the chip. This requires a total exposure time of 3000 s (1500 on the object and 1500 on the sky). We find that shorter exposures and more frequent chopping do not improve the quality of the data sufficiently to warrant the additional associated overhead.

Overhead required for telescope movement and guider communication is minimized by having all of the operations performed automatically by a command script that passes information to the auto-guider, telescope control system, and CCD electronics. The net overhead is approximately 5 minutes for the 3000 s procedure just described. Besides reducing the read-noise contribution to the total noise in the low light level portions of the image, the time saved in avoiding CCD reads after each sub-exposure is considerable ($\sim$ 30 s per readout), as is the time saved in data processing afterwards.

It is possible to symmetrize the galaxy–sky observing sequence by splitting the first integration into two identical integrations, one performed at the beginning of the observation and one at the end of the chopping sequence before the chip is read. This procedure is summarized in flow chart form in Fig. 2.

3. OBSERVATIONS

We tested this observing strategy and obtained data for several galaxies at the Michigan-Dartmouth-MIT (MDM) Observatory during a week of dark nights in 1995 June. We used the 2.4-meter Hiltner telescope equipped with the MDM Modular Spectrograph (ModSpec). The ModSpec has multiple observing modes that provide a variety of different instrumental resolutions, wavelength coverages, grating selections, and slit options. We observed with a 1200 *l*/mm reflection grating in first order and a thinned, backside-illuminated Tektronix 1024^2 CCD mounted at the focus of the short (85 mm, *f*/1.2) camera port. The spectrograph slit was stopped down in the spatial direction to approximately 6.7′ for all observations. The 24 μm pixels of the CCD correspond to $\approx$ 1.4″ on the sky. We opened the slit to a width of approximately 5″ for all observations. This provided a 3-pixel FWHM resolution of $\sim$6.4 Å , or $\approx$360 km s^{-1} at 5400 Å , which is sufficient to obtain velocity dispersions in the galaxies studied.

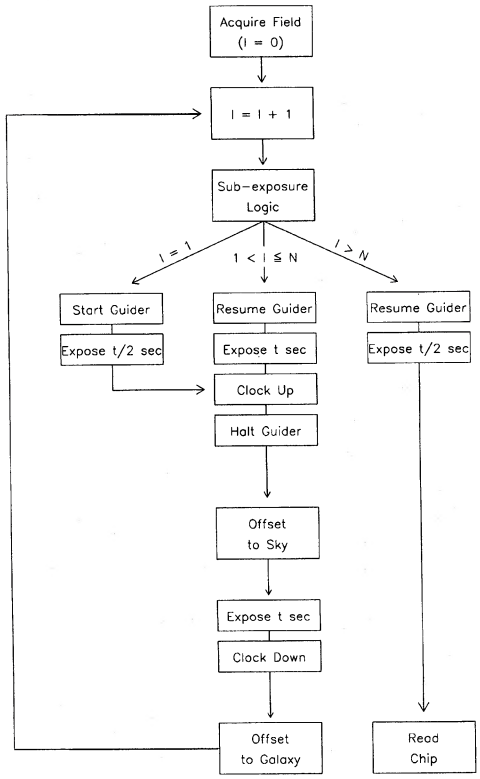

FIG. 2. A flow chart of a symmetrized version of the observing strategy outlined in the text. Note that one of the galaxy exposures has been divided into halves to be done at the beginning and end of the series of observations.

The wavelength region observed spans the 2200 Å interval from ~4300 Å to ~6500 Å. We selected this spectral region because it is near the 5000 Å blaze wavelength of the grating and because there are relatively few stellar lines of interest at wavelengths longer than the Na I $_D$ lines until Hα at 6563 Å. Tilt plates on which the CCD dewar mount compensate for the chromatic aberration introduced by the spectrograph camera optics at these wavelengths. The wavelength region observed contains the easily recognized Hβ, Mg I$_b$, and Na I$_D$ lines as well as many other stellar features (mainly Fe and other metal lines) suitable for cross-correlation analyses. Prominent night sky features at these wavelengths include (but are not limited to) an ensemble of emission lines from Hg I at 4358, 5461, 5770, and 5791 Å, the very strong O I line at 5777 Å, the Na I lines at 5890, 5896 Å, and the O I lines at 6300, 6364 Å.

In addition to galaxy and sky spectra, we also obtained wavelength calibration spectra produced by a combination of Ne, Ar, and Xe lamps immediately before and after each science observation. Flats, darks, and biases were obtained at the beginning and/or end of each night. Radial velocity standard star spectra were obtained by observing HD 132737 (K0 III) or HD 212943 (K0 III–IV) at different airmasses each night. The stars were trailed diagonally across the slit at a constant rate to provide uniform illumination of the slit. The calibration and standard star spectra were obtained at the same location on the CCD as the science exposures, but without chopping.

In this paper we will concentrate on the data obtained for three galaxies: M87, NGC 5846, and IC 1101. The galaxies were observed under different seeing conditions, zenith angles, and sky brightnesses. The data therefore provide a sampling of the types of observing conditions encountered when trying to determine the sky contribution to the galaxy spectrum. M87 and IC 1101 are giant elliptical galaxies at the centers of clusters, and NGC 5846 and NGC 5846A are companion galaxies in a small group. Being nearby, M87 fills the slit completely, as does NGC 5846 though to a lesser surface brightness level. IC 1101 fills only a portion (~ 1′) of the slit, but since it is located in a rich cluster, there is light from other objects entering at different slit positions. We summarize the observations in Table 1.

4. DATA REDUCTION

Each CCD image obtained contains two composite long-slit spectra, one for the galaxy (with corresponding sky) and one of the nearby sky field. We removed the bias level (~1000 ADU) applied to each image during readout by subtracting a smoothed version of the averaged overscan region of each frame. Cosmic rays were identified by an algorithm that stacks and scales the images for a given object into a data cube and then searches for deviant upward noise excursions within each stack of pixels in the cube. This identification process results in a mask containing the locations of spurious pixels in each image. This mask was used to clean the flagged pixels by quadratic interpolation in the spatial direction only, so as to preserve the spectral resolution at all points in the image. We inspected each individual cleaned image by eye and interactively removed those cosmic rays that were not cleaned automatically. These stray noise events most often occurred at the edges of the night sky lines because the light gradient is steep at these locations and the auto-cleaning algorithm is conservative in flagging pixels as being contaminated. Typically, about 0.5% of the pixels in

TABLE 1. Observing summary.[a,b]

Galaxy	RA (1950)	DEC (1950)	Type	PA	B_T (mag)	r_e (″)	Exp. (min)	Comments
M87	12^h 28.3^m	+12° 40′	E0/E1	−30°	9.59	95	300	Galaxy fills slit, large airmass
NGC 5846	15^h04.0^m	+01°46′	E0/E0	3°	11.59	63	500	Dark, good seeing, N5846A in slit
IC 1101	15^h08.4^m	+05° 56′	cD	34°	13.93	42	500	Partial moon rising, seeing variable

[a]Listed are the 1950 equatorial coordinates, morphological classification, position angle used for the observations, photoelectric total magnitude, effective radius, total exposure time, and observing comments.

[b]Data for M87 and NGC 5846 are from the RC3 (de Vaucouleurs *et al.* 1991), where r_e = A$_e$/2. Data for IC 1101 are from Peletier *et al.* (1990) and Fisher *et al.* (1995).

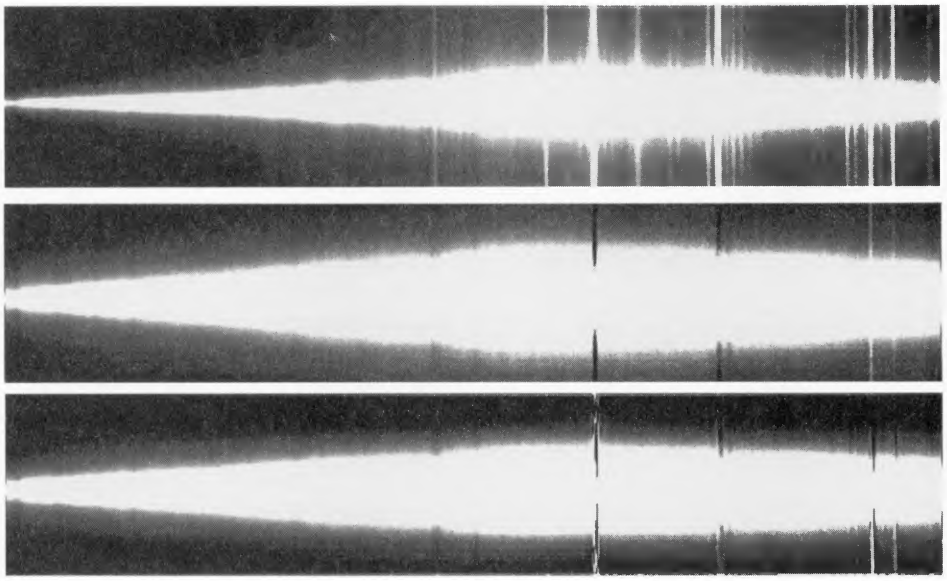

FIG. 3. (*Top*) Rectified long-slit spectrum of M87. The night sky has not been subtracted from this image. The wavelength range runs from ~4300 Å (left) to ~6500 Å (right). The strongest sky line just to the right of center is O I λ5777. (*Middle*) Sky-subtracted long-slit spectrum of M87 created using our sky subtraction method. The image intensity has been stretched to bring up faint, residual sky features that are not completely removed through the subtraction. (*Bottom*) Sky-subtracted long-slit spectrum of M87 created using the slit ends for estimating the night sky levels. The image intensity stretch is identical to that in the middle panel. The sky subtraction is poorer in this case than it is for our observing strategy. In particular, numerous weak night sky lines are present in this panel; these lines are removed effectively with our sky subtraction method shown in the middle panel. Note also that the brightness of the image near the slit ends is reduced below what it should be since the galaxy fills the slit.

each image were flagged for cleaning. This is consistent with the cosmic ray accumulation expected for the Tek chip used for the observations.

Next, we sectioned each image into its corresponding galaxy and sky portions and flatfielded each with a normalized flatfield frame produced by averaging 15–20 dome flat spectra. The dome flats were produced by observing a flatfield screen illuminated from behind by incandescent light passed through blue glass to reduce the red–blue color gradient in the lamp spectrum.

For each image, we then calculated the two-dimensional wavelength solution using the averages of the NeArXe exposures obtained at the telescope immediately before and after each science image. The arc lines were identified using standard line lists available from the lamp manufacturer as well as the MIT wavelength tables (Harrison *et al.* 1969). The fits to the lines were made using 2*D* cubic polynomials, which provided an rms accuracy of approximately 0.25 pixels, or 30 km s^{-1}. The slit position within each image was also mapped with cubic polynomials by using an image of a standard star spectrum obtained at incremental positions along the slit. The rms accuracy of the slit position determinations was about 0.23″.

The sky lines were removed from each galaxy image by simply subtracting the corresponding two dimensional sky image. These sky-subtracted images were then rectified and rebinned to a logarithmic wavelength scale using the wavelength solutions and slit position masks made previously. We also binned the images in the spatial direction into 2″ bins with minimal loss of resolution. As a last step, the individual images for each object were summed to produce a final data image.

The data reduction procedure for the standard star frames was simpler because sky line contamination during the exposures was minimal. Cosmic rays were removed from each image interactively. After applying the wavelength and slit position solutions, each image was collapsed in the spatial direction into a linear array for comparison with the reduced galaxy images.

5. QUALITY OF SKY SUBTRACTION

An example of our reduced sky-subtracted image for M87 is shown in the middle panel of Fig. 3. The top panel is a geometrically rectified image of the total long-slit spectrum of the galaxy in which the sky lines have not been removed so that their locations are obvious. The middle panel is a sky-subtracted image made using our chopping technique. The bottom panel in the figure is a second sky-subtracted version of the top panel made by estimating the sky strength in 10 pixel (~20″) regions at both ends of the slit. The image scalings of the middle and bottom panels are identical and are stretched to accentuate the properties of the images at low light levels. Comparison of the two panels shows that the residual contamination due to improper subtraction of the night sky lines is more noticeable when the sky is measured at the ends of the slit. This is most readily visible for the strong sky lines, but more importantly, it is also true for the myriad weaker sky lines throughout the spectrum. It is these weak sky lines that confound searches for common features in cross-correlations between program and template spectra. (Even with our technique, the strongest sky lines are not totally removed; the wavelength regions immediately surrounding the strongest lines are usually ignored in scientific analyses since these lines are so difficult to remove completely.) Another important aspect of Fig. 3 that should not

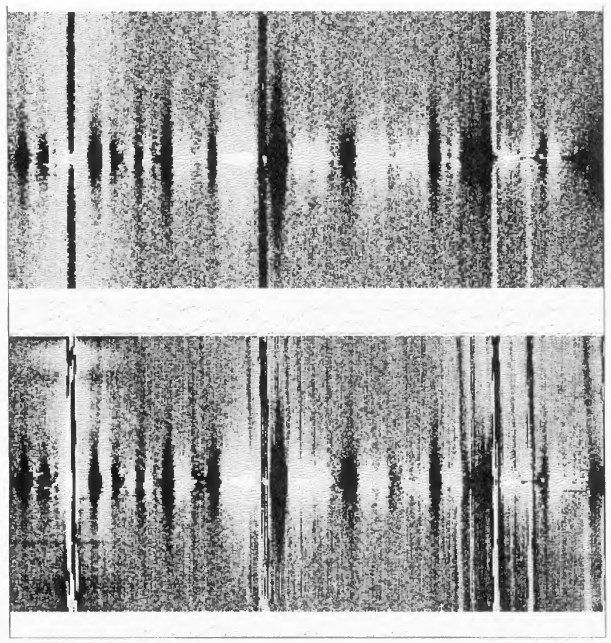

FIG. 4. Enlarged section of the sky-subtracted images shown in Fig. 3. (*Top*) Our method. (*Bottom*) Sky removed using ends of slit. We have removed the overlying galaxy spectrum in each panel by subtracting smoothed versions of the images created with a 50×0.5 pixel Gaussian filter. Absorption lines in the galaxy that have not be been completely removed by the smoothing appear as broad dark features. Note the numerous additional (narrow) sky lines visible in the bottom panel that are not seen in the top panel (note also the horizontal blemish in the lower left). The image stretch in both panels is identical. The wavelength range shown is ~5480 Å to ~6500 Å .

go unnoticed is that the middle panel containing our sky-subtracted image shows that the envelope of M87 fills the slit used for the observations. When the sky is estimated at the slit ends and subtracted from the image in the bottom panel information in these outer regions is lost.

In Fig. 4 we show an enlarged region of the middle and bottom panels of Fig. 3 after removing the overlying galaxy spectrum in each panel. The galaxy contribution was removed by subtracting smoothed versions of the images created by filtering the data with a 2*D* Gaussian filter of width 50 by 0.5 pixels. This process exposes the residual sky lines in each image and clearly shows that our sky subtraction method produces a cleaner spectrum.

Before discussing how much of an improvement in the sky subtraction can be made with our background subtraction method, we list some of the problems that can affect sky determinations.

(1) *Geometrical image distortion*. For our observations, there is a substantial curvature introduced in the image of the slit on the detector by the spectrograph optics. The curvature has an amplitude of about 2 pixels (~1.4%) over the 140 pixel distance from the middle to ends of the slit. Even precise geometrical rectification of the image can result in small relative shifts of the sky lines from one position to the next; shifts as small as ~ 0.05–0.10 pixel can lead to a poor subtraction, especially for strong sky lines. Image distortion can also be produced if the detector is not flat, though this is not the case for our observations.

(2) *Spectrograph flexure*. Exposures at large zenith distances are subject to the effects of instrumental flexure caused by the changing center of mass of the telescope/instrument during an observation. Flexure may introduce geometrical distortions into the position of the slit on the detector. These distortions can be difficult to remove; see (1).

(3) *Quality of flatfielding*. Observing sky and object with different detector pixels requires higher quality flatfielding than if the object and sky are observed with the same pixels. Uniform illumination of the slit can be difficult to achieve since the extended source observed for flatfield frames is not located at infinity.

(4) *Slit contamination or filling*. For extended objects that fill the slit (e.g., M87), it may not be possible to make a truly reliable estimate of the sky background from the data at the ends of the slit. In other cases, there may be contamination of ''sky'' regions of the slit by other objects; this can be particularly troublesome for observations of galaxies in rich clusters (i.e., IC 1101).

(5) *Time variability of sky lines*. Emission from the night sky varies on time scales shorter than most spectroscopic observations of faint astronomical objects. The most obvious way to circumvent this limitation is to observe the sky and object simultaneously (taking the sky from the ends of the slit) or by chopping between the galaxy and sky. We have found that 300 s subexposures are nearly optimal for the chopping procedure described in this paper. Shorter subexposures require greater overhead for a total exposure length, and longer subexposures do not adequately follow the changes in the night sky line strengths. Since the strengths of individual night sky lines do not change simultaneously, chopping has a distinct advantage over back-to-back object and sky exposures of long duration.

Our sky-subtraction method reduces or eliminates the problems described in points (1)–(5) above. We can quantify how much better we are doing with our observing strategy by considering how much noise is contributed by residual sky lines to a spectrum extracted from a sky-subtracted image. Let $\epsilon(i)$ be the standard deviation of the difference between the extracted spectrum in a given row i and the same extracted spectrum smoothed by n pixels:

$$\epsilon(i)=\sqrt{\frac{\Sigma_{j=1}^{N}(y_j-y_j\otimes F_n)^2}{(n-1)}}.$$

We take the smoothing function, F_n, to be a simple median filter of width $n=10$, and allow the sum to run over all points, j, in the extracted spectrum. The functional form of F_n, whether it be a median filter, boxcar filter, Hanning filter, etc., is not important as long as the filter width is large compared to the sky line widths and small compared to the spectral line widths.

The relative values of $\epsilon(i)$ obtained for images that have been sky-subtracted with the traditional slit method and with our chopping technique give an indication of the relative signal-to-noise ratios attainable with the two methods. We plot the values of $R(i)=(\mathrm{S/N})_{\mathrm{chop}}/(\mathrm{S/N})_{\mathrm{slit}}\approx\epsilon_{\mathrm{slit}}(i)/\epsilon_{\mathrm{chop}}(i)$ as a function of slit position for our M87 and NGC 5846 data in the top panels of Fig. 5. The two curves shown in the top panels are the values of $R(i)$ when two different regions of the slit are used to estimate $\epsilon_{\mathrm{slit}}(i)$. The general behavior of the curves is similar; there are minima near those positions

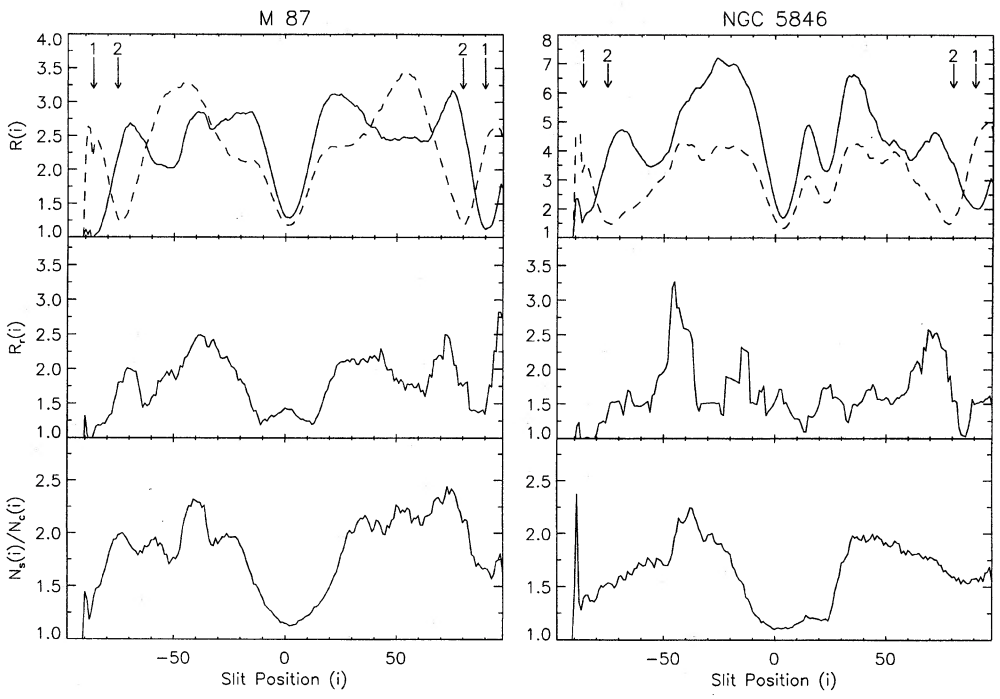

FIG. 5. Values of $R(i)$, $R_r(i)$, and $N_{slit}(i)/N_{chop}(i)$ for the M87 data (left) and NGC 5846 data (right). $R(i)$ and $R_r(i)$ are estimates of the relative signal-to-noise ratios in the sky-subtracted images obtained using our observing strategy compared to taking the sky from the slit ends. As expected, these quantities are greater than unity. The two cases shown in the top panel are for two different estimates of the sky obtained from the slit ends; the locations of the sky regions at the ends of the slit are marked with arrows. $N_{slit}(i)/N_{chop}(i)$ is the ratio of the number of points in each spectrum having an excursion from the mean spectrum intensity by more than a given threshold (see text).

of the slit used to determine the sky brightness and a minimum near the nucleus of the galaxy, where the signal is high compared to the residual sky background. Note that $R(i)>1$ everywhere, demonstrating the better sky subtraction possible with our method.

Much of the contribution to $R(i)$ comes from the residual contributions of the most prominent night sky lines in the extracted spectra. Since wavelengths near these strong lines are usually omitted from cross-correlation analyses, it is desirable to focus attention on the contribution by the numerous weaker sky lines throughout the spectral range used in the analyses. Removing the strongest sky lines from consideration by omitting the 4% of pixels that contribute most to ϵ_{slit} and ϵ_{chop} (i.e., a 2σ clipping), one finds a somewhat reduced value of the relative signal-to-noise ratios, $R_r(i)$. We plot $R_r(i)$ in the middle panels of Fig. 5 for the case where the sky is taken from the very ends of the slit (i.e., the solid line case in the top panels). As expected, $1<R_r(i)<R(i)$.

An alternate way to estimate the relative quality of the two techniques is to count the number of pixels in each extracted spectrum that contribute to the noise at a level greater than a given threshold, say $2\epsilon_{chop}(i)$. Values of this ratio, $N_{slit}(i)/N_{chop}(i)$, are plotted in the bottom panels of Fig. 5. For a 1024 pixel spectrum, $N_{chop}(i)$ is $\approx$ 45 pixels. Approximately twice as many pixels are affected in the spectrum obtained using the slit ends for sky estimation.

The main conclusion to be drawn from the plots in Fig. 5 is that our chopping method provides a background subtraction across the full width of the slit that is better than that obtained from the traditional approach. The S/N ratio of the data using this technique is often a factor of 2 or more higher than that obtained using the slit ends to estimate the sky. The increase in S/N obtainable significantly outweighs the cost of the additional observing time incurred (a factor of 2) in using the technique unless the object being studied is very bright or the exposure very short.

Since systematics can easily dominate at low light levels, it is unlikely that longer exposures will significantly improve the sky subtraction at low surface brightness when using the ends of the slit to obtain sky information. With our method, however, we have apparently not yet reached this point of diminishing returns after 8 hours of integration, so it should be possible to continue to further improve the signal-to-noise in the data by increasing the observing time.

6. REDSHIFTS AND VELOCITY DISPERSION PROFILES

We now present the results of our investigation into the velocity dispersions of the three galaxies. In Fig. 6 we show the light profile, redshift (cz), and velocity dispersion as a function of angular distance from the center of each galaxy. The corresponding linear distances and V-band surface brightnesses at several values of $r(")$ are provided for each object in Table 2. The light profiles are normalized summations of cuts perpendicular to the dispersion axis of spectrum. Redshifts and velocity dispersions were derived using standard cross-correlation (Tonry & Davis 1979; Statler

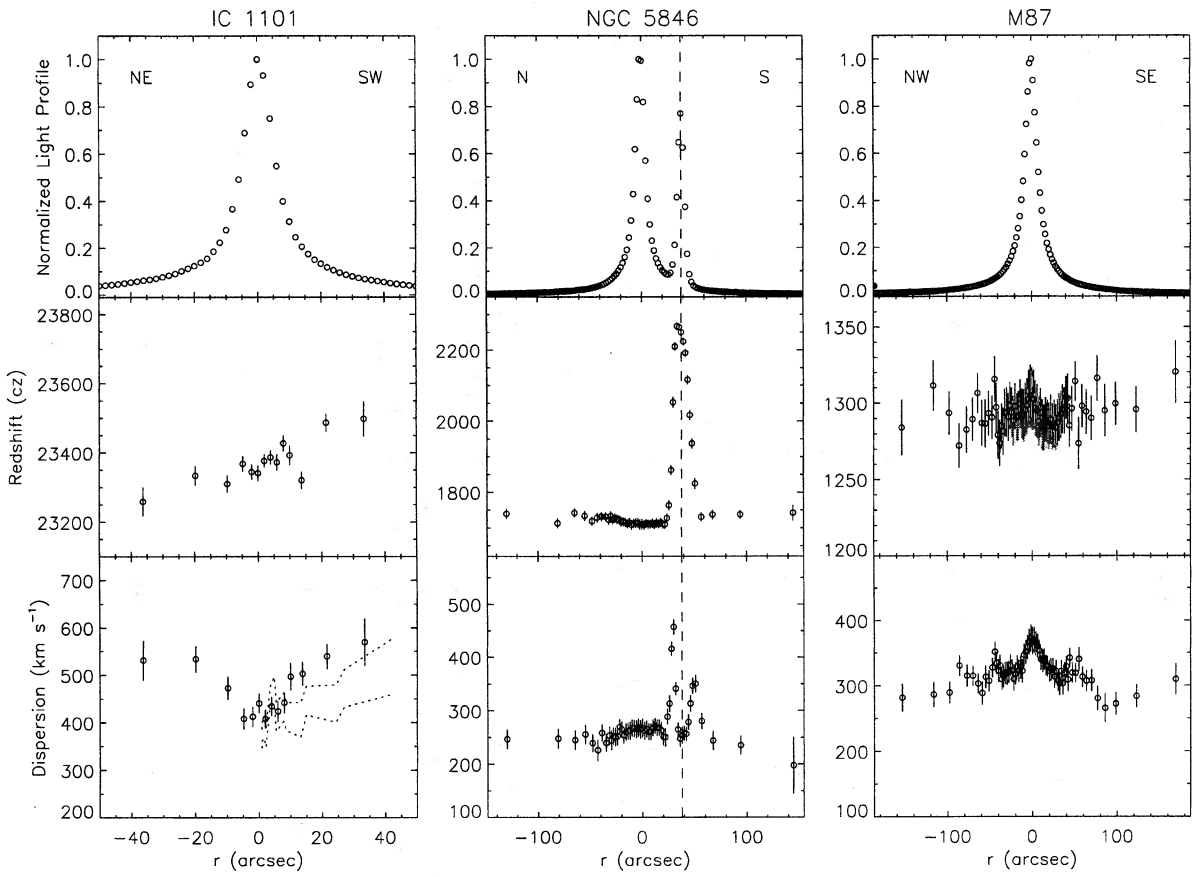

FIG. 6. Light profiles, redshift (cz) profiles, and velocity dispersion profiles for IC 1101, NGC 5846, and M87. The values are error-weighted averages of the results from cross-correlation and Fourier quotient analyses. Equivalent linear sizes for the angular scales shown can be found for each galaxy in Table 2. The vertical dashed line in the middle panels indicates the position of NGC 5846A, the companion to NGC 5846. The short dashed lines in the bottom panel for IC 1101 indicate the range of dispersion values found by Dressler (1979). Note that our values are ≈7%–10% higher as discussed in the text.

1995) and Fourier quotient (Sargent *et al.* 1977; Whitmore 1980; Larsen *et al.* 1983; Laird & Levison 1985) techniques. The results shown are error-weighted averages of the cross-correlation and Fourier quotient results. Wavelength regions nearest the strong sky lines of Hg I, Na I, and O I (see Sec. 3) were excluded from the calculations. Values of V_r and σ_r obtained from different standard star comparisons were indistinguishable.

Our velocity dispersion results compare reasonably well to the average values listed in the literature. Whitmore *et al.* (1985) list values of 241–262 km s^{-1} for NGC 5846, 375 ± 13 km s^{-1} for IC 1101 (see Dressler 1979), and 315–358

TABLE 2. Surface brightnesses of the objects studied.[a]

	M87 (d≈16 Mpc)		NGC 5846 (d≈27.5 Mpc)		IC 1101 (d≈311 Mpc)[b]	
r (″)	r (kpc)	μ_V (mag arcsec^{-2})	r (kpc)	μ_V (mag arcsec^{-2})	r (kpc)	μ_V (mag arcsec^{-2})
20	1.6	19.10	2.7	20.17	30	20.15
40	3.1	20.29	5.3	20.84	60	24.00
60	4.7	20.92	8.0	22.07	...	...
80	6.2	21.47	10.7	22.63	...	...
100	7.8	21.88	13.3	23.06	...	...
150	11.6	23.54	20.0	23.97	...	...

[a]Surface brightness estimates for M87 and NGC 5846 are from V-band images obtained by the authors. Values for IC 1101 are from Malumuth & Kirshner (1985).
[b]The distance for IC 1101 was calculated from the observed redshift assuming H_o = 75 km s^{-1} Mpc^{-1}.

km s^{-1} for M87. We find values of ~265 for NGC 5846, ~382 km s^{-1} for IC 1101, and ~350–370 km s^{-1} in the inner regions ($r<20$)″ of M87. The zero point of our dispersions appear to be about 6%–7% higher than the average literature values. We have used a large slit to obtain as much light as possible at large radii, which in combination with small velocity effects due to spectrograph flexure could account for this broadening. Since the focus of this paper is to demonstrate that the observing method outlined yields accurate *relative* velocity results as a function of position, we have not made any attempt to compensate for this small broadening in Fig. 6.

The data shown in Fig. 6 extend out to approximately one effective radius for IC 1101 and two effective radii for M87 and NGC 5846. For NGC 5846 and IC 1101, we reached a *V*-band magnitude of 24, which is 2.2 mag below the average dark sky levels at MDM Observatory.

M87: M87 is the large elliptical galaxy at the center of the Virgo cluster and has been the subject of numerous investigations relating to various aspects of the galaxy. Dressler & Richstone (1990) have studied the kinematics of the stellar content within the inner few arc second core of the galaxy. However, as far as we know, there have been no thorough studies of the stellar kinematics in the outer regions of the galaxy. Our data indicate that the velocity dispersion declines out to r ≈ 100″, but that it may thereafter remain constant. We will shortly obtain additional measurements over a much larger angular distance to see if this result can be verified.

IC 1101: The bright central galaxy in Abell 2029, IC 1101, has a large cooling flow (Stewart *et al.* 1984). It is classified as a cD galaxy, though it lacks the usual cD halo (Porter *et al.* 1991). Dressler (1979) first noted that this galaxy shows evidence for a rising velocity dispersion with increasing galactocentric distance. We confirm this result over roughly the same galactocentric radii as he observed. A linear fit of the form $\log \sigma_r = A_{\sigma,r} \log r + B_{\sigma,r}$ to the data shown in Fig. 6 for $r<40''$ yields $A_{\sigma,r} = +0.086 \pm 0.014$ and $B_{\sigma,r} = 2.594 \pm 0.012$. This 6σ positive slope detection in $A_{\sigma,r}$ is in agreement with the value of $+0.068 \pm 0.017$ found for Dressler's data by Davies & Illingworth (1983) as well as the value of 0.096 ± 0.025 reported by Fisher *et al.* (1995) for the inner 11″ of the galaxy. The only other early-type galaxy for which there appears to be a bona fide non-decreasing velocity dispersion at large radii is NGC 7144. By observing with the European Southern Observatory 3.5 meter NTT for 522 minutes, Saglia *et al.* (1993) were able to trace the velocity dispersion profile in NGC 7144 out to $\approx 2r_e$, which corresponds to a *B*-band surface brightness of 24.4 mag arcsec^{-2}. They find that σ_r in this galaxy remains flat or perhaps rises slowly out to this radius.

Our data indicate that the outer regions of IC 1101 rotate with a velocity of ~110–120 km s^{-1}. This result was also tentatively identified by Dressler (1979). However, contrary to his conclusion that there is no evidence for rotation in the inner regions, we find a fairly smooth progression in rotation velocity as a function of radius. In both studies, the slit was oriented along the major axis of the galaxy.

NGC 5846: NGC 5846 is a large elliptical galaxy at the center of a dense, symmetric group of galaxies within the Local Supercluster (Haynes & Giovanelli 1991). The galaxy exhibits strong x-ray emission (Fabbiano *et al.* 1992) and is thought to have a central cooling flow (Canizares *et al.* 1987). The galaxy may have a mass comparable to that of M87 (Biermann *et al.* 1989), but searches for cool gas associated with the cooling flow indicate that the properties of its extended hot gas envelope may be more similar to that of the large Virgo elliptical NGC 4472 (Bregman *et al.* 1988; Fabbiano *et al.* 1989).

There is little known about the velocity dispersion profile for this galaxy at large radii. Our data represent the first measurements out to two effective radii (~ 20 kpc). We chose a position angle of 3° for the observations since this allowed us to place NGC 5846A, which is 40″ south of NGC 5846, in the slit as well. This slit position corresponds closely to the minor axis of NGC 5846. Previous authors have observed the inner regions of the galaxy, but the velocity dispersion profiles generally extend only to $r<15''$–$20''$ (e.g., Franx *et al.* 1989). A linear fit the velocity dispersion profile shown in Fig. 6 between $-140''<r<0''$ yields $A_{\sigma,r} = -0.026 \pm 0.012$ and $B_{\sigma,r} = 2.441 \pm 0.012$, which is only marginally inconsistent with a flat profile out to $2r_e$. At a radius of 100″ (~12–14 kpc) the inferred velocity dispersion is consistent with the dark matter velocity dispersion $\sigma_{DM} \approx 244 \pm 4$ km s^{-1} predicted by Kochanek (1994) for an isotropic velocity dispersion tensor ($\beta = 0$) assuming the galaxy is spherical and non-rotating. We will present a complete analysis of the data for this galaxy together with optical and x-ray imaging in a forthcoming paper.

In Fig. 6 there is mixing of the light from NGC 5846 and its companion NGC 5846A. In the dispersion and radial velocity profiles this leads to a combination of the results for the two galaxies at some radii. We have indicated the position of NGC 5846A with a vertical dashed line. Values within a few points of this line should provide accurate estimates for the quantities associated with NGC 5846A. The next several closest values represent blended results that lead to the "spikes" seen in the dispersion profile. The velocity dispersion of NGC 5846A is quite high for a galaxy of its luminosity, and it is an example where the "fundamental plane for early-type galaxies," which accounts for density as well as luminosity and dispersion, does better than the Faber–Jackson relation. Perhaps because of its history as a companion of NGC 5846, NGC 5846A is more compact and therefore has a higher velocity dispersion than galaxies of similar luminosity.

7. THE SEARCH FOR DARK MATTER AND THE ORIGIN OF ELLIPTICAL GALAXY ENVELOPES

Information about the internal kinematics of many early-type galaxies exists, but relatively little is known about the dynamics of the outer envelopes at very large radii from optical spectroscopy. The best studied case is that of the giant cD at the center of Abell 2029. Dressler (1979) has shown that the velocity dispersion of the galaxy increases as a function of radius out to about $50h^{-1}$ kpc. IC 1101 appears to be a normal elliptical ($M/L \approx 10$), which has accreted a

large amount of material that has inflated a luminous halo ($M/L \approx 35$). Furthermore, the galaxy may be embedded in a substrate of a dark ($M/L \approx 500$) intracluster medium. CDs may strip material from neighboring galaxies passing through their outer envelopes (Ostriker & Tremaine 1976) and may accumulate pre-stripped material sitting in the potential well of the cluster (Richstone 1976; Malumuth & Richstone 1984). The increasing dispersion in IC 1101 would appear to favor some such accumulation of material in the halo of the galaxy. For a review of the properties and origin of CD galaxies, see Tonry (1987).

A dark matter halo is, however, not the only possible interpretation for a rising velocity dispersion. Tonry (1983) has shown that the IC 1101 data can be fitted with a constant *M/L* model provided that the velocity dispersion is anisotropic. A possible means for distinguishing between the various possible contributions to σ_r is to combine the stellar kinematical data with information about the gravitational potential traced by x-ray emitting gas in the galaxies. Such measurements in and of themselves can be used to constrain the intrinsic shapes, baryon fractions, and dark matter distributions (Buote & Canizares 1996a,1996b), but they are much more powerful when combined with stellar kinematics information (see de Paolis *et al.* 1995).

One scientific issue that needs to be addressed is whether a result similar to that for IC 1101 (i.e., a velocity dispersion increasing with galactocentric radius) holds for other cD galaxies at the centers of rich clusters. As noted above, NGC 7144 shows evidence for a non-decreasing velocity dispersion profile out to $\sim 2r_e$. Carter *et al.* (1985) also find a non-decreasing dispersion in several CD galaxies in moderately rich clusters (IC 2082, Sersic 40/6, PKS 2354−35, 0539−40) out to about one effective radius and an *R*-band surface brightness of 22.8–24.3 mag arcsec^{-2}. Several other studies also indicate that the velocity profiles are flat or declining slowly with radius (Carollo *et al.* 1995; Statler *et al.* 1996). It is important to note that there is some disagreement about the character of the dispersion profile at large radii for some galaxies. For example, Saglia *et al.* (1993) find a relatively flat velocity dispersion profile out to $\sim 1r_e$ for the Virgo elliptical NGC 4472, while Fisher *et al.* (1995) note a decline over a slightly larger range in radius. These differences in the determinations of the velocity dispersion profile at values of $r \geq r_e$ could be due to difficulties in removing the sky background. Both Fisher *et al.* and Saglia *et al.* suggest that new detector/spectrograph configurations may be needed to resolve this issue.

The observing method described in this paper allows these types of measurements to be obtained with existing equipment now. We have shown that it is possible to do so even with modest aperture telescopes. Implementation of the method on larger telescopes would allow meaningful statistical comparisons between different classes of galaxy or cluster environments to be made within reasonable observing allocations.

We thank Mark Metzger for help with the software used to control the CCD electronics during the observations and the staff of the MDM Observatory for their assistance with the instrumentation setup. We thank John Blakeslee for reading a draft of the manuscript and for providing useful comments.

REFERENCES

Biermann, P.L., Kronberg, P.P., & Schmutzler, T. 1989, A&A, 208, 22
Bregman, J.N., Roberts, M.S., & Giovanelli, R. 1988, ApJ, 330, L93
Buote, D.A., & Canizares, C.R. 1996a, ApJ, 457, 177
Buote, D.A., & Canizares, C.R. 1996b, ApJ, 457, 565
Canizares, C.R., Fabbiano, G., & Trinchieri, G. 1987, ApJ, 312. 503
Carollo, C.M., de Zeeuw, P.T., van der Marel, R.P., Danzinger, I.J., & Qian, E.E. 1995, ApJ, 441, L25
Carter, D., Inglis, I., Ellis, R.S., Efstathiou, G., & Godwin, J.G. 1985, MNRAS, 212, 471
Davies, R.L., & Illingworth, G. 1983, ApJ, 266, 516
de Paolis, F., Ingrosso, G., & Strafella, F. 1995, ApJ, 438, 83
de Vaucouleurs, G., de Vaucouleurs, A., Corwin, H.G., Buta, R.J., Paturel, G., & Fouque, P. 1991, Third Reference Catalogue of Bright Galaxies (Springer, New York)
Dressler, A., 1979, ApJ, 231, 659
Dressler, A., & Richstone, D.O. 1990, ApJ, 348, 120
Fabbiano, G., Gioia, I.M., & Trinchieri, G. 1989, ApJ, 347, 127
Fabbiano, G., Kim, D.-W., & Trinchieri, G. 1992, ApJS, 80, 531
Fisher, D., Illingworth, G., & Franx, M. 1995, ApJ, 438, 539
Franx, M., Illingworth, G., & Heckman, T. 1989, ApJ, 344, 613
Harrison, G.R., *et al.* 1969, The Massachusetts Institute of Technology Wavelength Tables (MIT Press, Cambridge)
Haynes, M.P., & Giovanelli, R. 1991, AJ, 102, 841
Kochanek, C.S. 1994, ApJ, 436, 56
Laird, J.B., & Levison, H.F. 1985, AJ, 90, 2652
Larson, N., Norgaard-Nielsen, H.U., Kjaergaard, P., & Dickens, R.J. 1983, A&A, 117, 257
Malumuth, E.M., & Kirshner, R.P. 1985, ApJ, 291, 8
Malumuth, E.M., & Richstone, D.O. 1984, ApJ, 276, 413
Metzger, M.R., Tonry, J.L., & Luppino, G.A. 1993, in Astronomical Data Analysis Software and Systems II, edited by R.J. Hanisch, R.J.V. Brissenden, and J. Barnes (ASP, San Francisco)
Ostriker, J.P., & Tremaine, S.D. 1976, ApJ, 202, L113
Peletier, R.F., Davies, R.L., Illingworth, G.D., Davis, L., & Cawson, M. 1990, AJ, 100, 1091
Porter, A.C., Schneider, D.C., & Hoessel, J.G. 1991, AJ, 101, 1561
Richstone, D.O. 1976, ApJ, 204, 642
Saglia, R.P., *et al.* 1993, ApJ, 403, 567
Sargent, W.L.W., Schechter, P.L., Bocksenberg, A., & Shortridge, K. 1977, ApJ, 212, 326
Statler, T.S. 1995, AJ, 109, 1371
Statler, T.S., Smecker-Hane, T., & Cecil, G.N. 1996, AJ, 111, 1512
Stewart, G.C., Fabian, A.C., Jones, C., & Forman, W. 1984, ApJ, 258, 1
Tonry, J.L. 1983, ApJ, 266, 58
Tonry, J.L. 1987, in IAU Symposium 127, Structure and Dynamics of Elliptical Galaxies, edited by T. de Zeeuw (Reidel, Boston), p. 89
Tonry, J.L., & Davis, M. 1979, AJ, 84, 1511
Whitmore, B.C. 1980, ApJ, 242, 53
Whitmore, B.C., McElroy, D.B., & Tonry, J.L. 1985, ApJS, 59, 1